Nanoscale

Memristive plasticity in artificial electrical synapses via geometrically reconfigurable, gramicidin-doped biomembranes.

Journal:	*Nanoscale*
Manuscript ID	NR-ART-08-2019-007288.R1
Article Type:	Paper
Date Submitted by the Author:	23-Sep-2019
Complete List of Authors:	Koner, Subhadeep; University of Tennessee, Mechanical, Aerospace, and Biomedical Engineering Najem, Joseph; Pennsylvania State University, Department of Mechanical Engineering Hasan, Md. Sakib; University of Mississippi, Department of electrical engineering Sarles, Stephen; University of Tennessee, Mechanical, Aerospace and Biomedical Engineering

Memristive plasticity in artificial electrical synapses via geometrically reconfigurable, gramicidin-doped biomembranes

Subhadeep Koner[1], Joseph S. Najem[2], Md Sakib Hasan[3], Stephen A. Sarles[1]

[1] Department of Mechanical, Aerospace and Biomedical Engineering, University of Tennessee, Knoxville, Tennessee 37916, United States;

[2] Department of Mechanical Engineering, The Pennsylvania State University, University Park, Pennsylvania 16802, United States;

[3] Department of Electrical Engineering, University of Mississippi, Oxford, Mississippi 38677, United States.

*Corresponding author:

Stephen A. Sarles, Department of Mechanical, Aerospace and Biomedical Engineering, University of Tennessee, 308 Dougherty Engineering Bldg., 1512 Middle Dr., Knoxville, TN 37996, Phone: 865-974-3488, email: ssarles@utk.edu

ABSTRACT

It is now known that mammalian brains leverage plasticity of both chemical and electrical synapses (ES) for collocating memory and processing. Unlike chemical synapses, ES join neurons via gap junction ion channels that permit fast, threshold-independent, and bidirectional ion transport. Like chemical synapses, ES exhibit activity-dependent plasticity, which modulates the ionic conductance between neurons and, thereby, enables adaptive synchronization of action potentials. Many types of adaptive computing devices that display discrete, threshold-dependent changes in conductance have been developed, yet far less effort has been devoted to emulating the continuously variable conductance and activity-dependent plasticity of ES. Here, we describe an artificial electrical synapse (AES) that exhibits voltage-dependent, analog changes in ionic conductance at biologically relevant voltages. AES plasticity is achieved at the nanoscale by linking dynamical geometrical changes of a host lipid bilayer to ion transport via gramicidin transmembrane ion channels. As a result, the AES uniquely mimics the composition, biophysical properties, bidirectional and threshold-independent ion transport and plasticity of ES. Through experiments and modeling, we classify our AES as a volatile memristor, where the voltage-controlled conductance is governed by reversible changes in membrane geometry and gramicidin channel density. Simulations show that AES plasticity can adaptively synchronize Hodgkin-Huxley neurons. Finally, by modulating the molecular constituents of the AES, we show that the amplitude, direction, and speed of conductance changes can be tuned. This work motivates the development and integration of ES-inspired computing devices for achieving more capable neuromorphic hardware.

INTRODUCTION

Two-terminal synaptic devices hold promise to store and process information at significantly lower energy cost than three-terminal devices[1-4]. By emulating threshold-dependent conductance

changes and multi-timescale memory and plasticity found in their biological counterparts, artificial synapses could radically transform computing hardware by mimicking the way the brain learns, remembers, and processes information through activity-dependent plasticity [5]—originally believed to be present only in chemical synapses. Accordingly, research to develop synapse-inspired computing devices has produced material systems, including non-volatile memristors [6-8] with hysteretic current-voltage relationships, that inherently mimic the discrete, threshold-dependent conductance switching used by chemical synapses.

In contrast, electrical synapses (ES) have long been thought to form fixed-conductance connections (modeled as fixed resistors) between neurons. However, it was recently reported that the magnitude of electrical coupling (i.e., proportional to synapse conductance) between neurons connected via electrical synapses can vary significantly through activity-dependent plasticity [9-11] to control the level of synchronization in neural networks. Similar to their chemical counterparts, ES exhibit multiple forms of plasticity (e.g., facilitation, depression) at timescales ranging from milliseconds to days [12]. For example, coupling between retinal photoreceptors can be very low in complete darkness or bright light and significantly elevated at moderate light intensities [13, 14]. This variation enhances the sensitivity of retinal circuits during transitioning between nighttime and daytime visual tasks.

ES are composed of gap junctions, aligned protein hemi-channels (e.g., connexins or innexins) contributed from adjacent cells [15, 16], that span the 2-4 nm gap between plasma membranes. These water-filled structures mechanically and electrically link neurons [17, 18] as illustrated in Figure 1A. Unlike the voltage-triggered release of neurotransmitters in chemical synapses, the pre-synaptic terminal of an electrical synapse does not have to cross a firing threshold to transmit an action potential [19]. Instead, ions diffuse passively through the always-open hemichannels to cells at lower potentials. The lack of a threshold enables quicker communication and sharing of action potentials. But, while always conductive, the conductance (i.e., coupling) of an electrical synapse is not static, but rather continuously variable. The coupling level between neurons is often measured as the ratio of voltages accumulated in both the pre- and postsynaptic neurons [20]. These dynamic variations in coupling levels instill modulation of both the temporal and spatial transmission of information exchange [21]. Mechanistically, electrical synapse plasticity can result from dynamic alterations of existing connexin conductance states [22-24], increases or decreases in number of connexin channels [25-27], and modification of passive and active membrane properties by synaptic inputs [28-31].

Undoubtedly, the superior cognitive ability of the brain stems from collective functionalities of networks of chemical and electrical synapses adapting and communicating together. However, brain-inspired materials and neuromorphic devices seeking to achieve signal processing, learning, and memory capabilities of the brain have predominately focused on two- or three-terminal devices (e.g., memristors, transistors) with voltage-controlled, threshold-dependent changes in electrical/ionic conductance [2]. The vast majority of these systems exhibit sharp threshold-dependent switching [32, 33] between a small number of discrete conductance states [6, 33-38], thereby implicitly mimicking the functionalities of chemical synapses [39, 40]. On the other hand, the development of threshold-independent synaptic devices with activity-controlled, analog changes in conductance has received far less attention [41].

Here, we present an artificial electrical synapse (AES) constructed with a 5 nm-thick synthetic bio-membrane containing voltage-independent, pore-forming gramicidin peptides. Like biological ES, this assembly permits bidirectional ion transport via always-open channels and exhibits voltage-dependent memory resistance, with continuous conductance variations that occur across nominal

ranges of 22-160 pS [16] and at biologically-relevant voltages. This contribution builds on our recent work [42], which demonstrated that insulating, lipid-only biomembranes formed between lipid-coated aqueous droplets in oil exhibit hysteretic, geometric reconfigurations stemming from voltage-driven modulation of membrane area and thickness. Introducing gramicidin peptides into the membrane creates always-conductive transmembrane ion channels similar to gap junctions—transforming the capacitive membrane into a memristive one that exhibits a pinched, hysteretic current-voltage relationship and displays short-term plasticity to successive voltage pulses. Experiments and modeling are performed to assess changes in membrane geometry and gramicidin channel densities in response to voltage and to explain the sources of resistance hysteresis and short-term plasticity. These allow us to show that the dynamic geometrical reconfigurations of the membrane dictate the rates of current-voltage hysteresis, even though the density of gramicidin channels also increases with applied voltage. Finally, we demonstrate through both experiments and modeling that the AES can be modularly configured to exhibit paired-pulse depression and that voltage-induced plasticity in conductance can synchronize the firing of Hodgkin-Huxley neurons.

RESULTS AND DISCUSSION

A gramicidin-doped lipid membrane has similar structure and composition to biological ES. Inspired by the biomolecular memristor featuring voltage-activated alamethicin channels [43] and the capacitive, lipid-only biomolecular memcapacitor [42], the artificial electrical synapse (AES) studied herein represents a modular variation of those prior embodiments, one that is also based on a planar lipid bilayer membrane formed at the interface between two lipid-coated aqueous volumes in oil (also known as a droplet interface bilayer (DIB), see Experimental). Specifically, the ~5 nm-thick, insulating membrane is doped with gramicidin peptides that spontaneously insert [44, 45] in the absence of voltage into the membrane where monomers in each leaflet align end-to-end to form water-filled, conductive channels across the membrane. Illustrated in Figure 1B, this end-to-end alignment and the resulting ionic conductivity achieved with gramicidin channels closely mimic the structural configuration and voltage-independent transport properties of connexins in ES. Also, like gap-junctions in ES, this AES is always in a conductive (active) state.

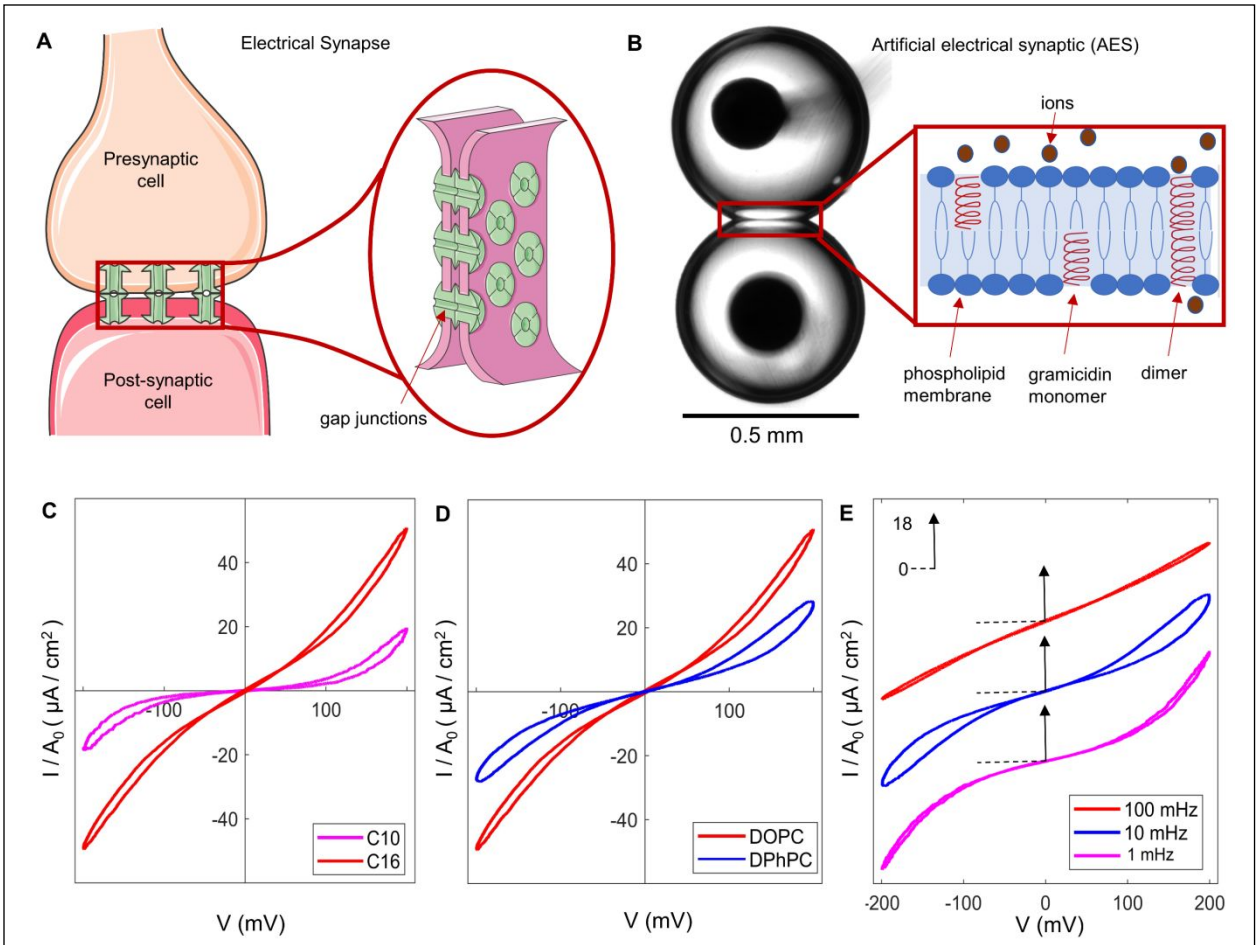

Figure 1. Two terminal AES exhibiting nonlinear memristive behavior. (A) Cartoon depicting ES gap junctions formed by connexin hemi-channels. (B) Biomolecular AES with gramicidin monomers dimerizing end-to-end to form channels for ion passage (inset) through the membrane. *I-V* relationships for: (C) DOPC AES assembled in two different oils: hexadecane (red) and decane (magenta); (D) AES formed in hexadecane from either DOPC or DPhPC lipids; and (E) DPhPC AES in hexadecane. All currents are normalized per zero-volt initial area, A_0. Applied bias consisted of a 200-mV bipolar sinusoidal voltage at 10 mHz, unless stated otherwise.

Current-voltage relationships reveal memristive behavior. The hypothesis motivating this study is that the voltage-dependent geometric reconfigurations we observe in lipid-only membranes provides a lever for affecting the number of gramicidin channels in the membrane to instill activity-dependent plasticity found in ES. Therefore, to characterize these responses and reveal the effects of lipid and oil types, we measure the current, *I*, induced by a sinusoidal voltage, *V*, on gramicidin-doped membrane s constructed separately from two types of synthetic lipids (diphytanoyl phosphatidylcholine, DPhPC, and dioleoyl phosphatidylcholine, DOPC) that form stable lipid bilayers [46] and two different alkane oils (hexadecane, C16, and decane, C10) that result in varying sensitivities to voltage-drive changes in membrane area and thickness [42]. Representative *I-V* responses for final gramicidin concentrations of 0.5 μM in each droplet are shown in Figure 1C-E, with the current normalized by the zero-volt membrane area to minimize effects of differing starting synapse areas.

For all combinations, we measure pinched, hysteretic *I-V* loops at frequencies less than 50 mHz. Figure 1C shows that DOPC AES in C10 exhibit stronger nonlinearity and larger hysteresis when compared to hexadecane. Moreover, the instantaneous slopes of these data show that the DOPC AES in C10 exhibits relatively higher ohmic resistance (86 kΩ-cm^2) near 0 V (flatter) and lower resistance (12 kΩ-cm^2) near |200 mV| (steeper). In C16, both DOPC AES and DPhPC AES exhibit less variation in resistance versus voltage: 10 kΩ-cm^2 and 17 kΩ-cm^2 near 0 V, respectively, to 6.6 kΩ-cm^2 and 9 kΩ-cm^2 near 200 mV, respectively. In comparison, lipid-only membranes lacking gramicidin exhibit significantly higher resistances of 10-100 MΩ-cm^2 and do not exhibit *I-V* hysteresis at frequencies below 50 mHz (see Figure S2). Since the conductance of a gramicidin channel is relatively constant (5.8 pS) [47, 48], this suggests the number of gramicidin channels per unit area in DOPC AES in C10 is less than in a DOPC AES in C16.

Figure 1D compares the responses of AES formed from the two different lipids types (DPhPC and DOPC) in C16. Here, we see that a DOPC AES displays less *I-V* hysteresis and higher conductance, signifying a higher gramicidin channel density than in DPhPC. This difference is consistent with and can explained by prior research which demonstrated that gramicidin channels have higher affinity for [49] and greater stability (i.e., channel lifetime) [50] in DOPC membranes compared to DPhPC bilayers.

These measurements also reveal the frequency of the applied voltage sweep affects shape and hysteresis of the *I-V* relationship. The representative data in Figure 1E for a DPhPC AES in C16 show that the *I-V* response is most nonlinear at the lowest frequency (1 mHz) and the most linear at 100 mHz. These data also show that hysteresis is minimal at both the lowest and highest frequencies tested and significantly greater at the middle frequency of 10 mHz. While not shown, the same trend is observed for membrane-based AES constructed with DOPC or using decane. The disappearance of hysteresis at very low frequencies demonstrates that resistive hysteresis in the AES is volatile.

Moreover, unlike our prior study [43] using alamethicin-doped membranes that exhibited strong voltage-dependent increases in conductance and high nominal OFF resistances (>1 GΩ, when channels fully exited the membrane), these data show that gramicidin membranes are always conductive (≤ 86 kΩ), even at low voltages—just like ES. These trends remain across gramicidin concentrations (see Figure S3), which merely scales the number of channels in the interface, proportionally increasing the conductance of the membrane.

Chua established that the fingerprint of a memristor is a pinched hysteresis loop on an *I-V* plane at certain frequencies and initial conditions when subjected to a voltage or current signal producing a periodic response of similar frequency [3, 51-53]. Therefore, the results in Figure 1 prove that a gramicidin-doped AES is a volatile memristor, one in which the *I-V* shape, hysteresis, and frequency range of memristance can be tuned based on membrane composition and also the oil type surrounding the droplets. In the context to synaptic plasticity, the hysteresis implies that the conductance of the membrane depends on its prior history of excitation, not just the present stimulus. And unlike the pinched, hysteretic *I-V* responses measured previously using alamethicin-doped membranes that exhibited exponential increases in current only at voltages above an insertion threshold for the peptides, these AES do not require a specific threshold to become conductive. The modulations in AES resistance are also continuously variable, unlike most solid-state memristors that demonstrate discrete switching [54].

Modelling gramicidin-doped membrane AES. As depicted in Figure 1C-E, gramicidin-doped membranes exhibit pinched and hysteretic current induced by a symmetric sinusoidal bias. Since the passage of ions is mediated by gramicidin dimers in the bilayer, these measurements indicate that nominal conductance of the membrane and thus the total number of dimers present depends on both voltage and time.

We know that the membrane elastically reconfigures in response to a nonzero membrane voltage [42, 55] . These reversible changes occur with time constants on the order of seconds and can result from formation of new membrane area due to electrowetting (EW) and a reduction in hydrophobic thickness caused by electrocompression (EC). While not explicitly linked, these geometrically changes are implicitly coupled by the fact that changes in membrane thickness modifies the effective forces driving both EW and EC [42]. The fact that our data show larger currents upon a decrease in voltage from some maximum value compared to an increase in magnitude of voltage from zero is consistent with the idea that a recent increase in membrane are driven by EW and a decrease in membrane thickness from EC could help to increase the total number of gramicidin dimers present in the interface. Another possibility is that the kinetics of gramicidin insertion, and thus the net number of channels present at equilibrium, are themselves functions of voltage (or membrane thickness) as is common in many other types of ion channels.

To properly identify and separate these mechanisms driving voltage-induced plasticity, we

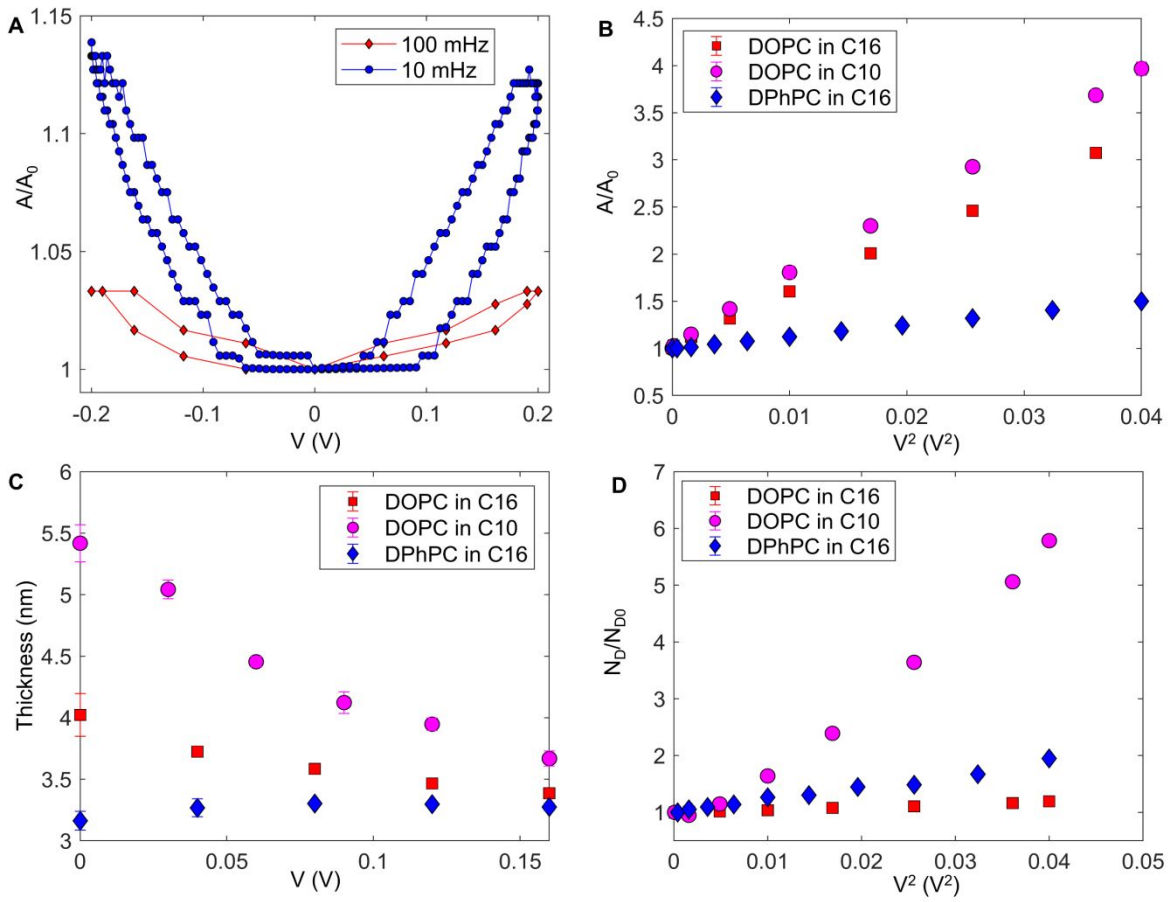

Figure 2. Characterization of the state variables at steady-state EW and EC conditions based of EW and EC time constants respectively. (A) Hysteretic geometric reconfiguration of the membrane interface when stimulated with a sinusoidal input bias voltage of 200 mV at different sweep rates, evaluated as mean of three (steady-state EW) cycles. (B) Response of the normalized area over initial area (at 0 mV) to step increase of bias voltage. (C) Relative thinning of the bio-membrane due to Electro-compression for different lipids in different oils in response to step increase in bias voltages. (D) Relative Channel density (normalized over 0 mV conditions) at the membrane interface for different lipid types in different oil environments.

Table 1: Summary of EW, EC, and gramicidin channel density dependencies on voltage

Membrane/Oil	EW area growth		EC thinning	Channel Density ($\times 10^6$)
	τ_{ew} (s)	$\alpha\ (V^{-2})$	τ_{ec} (s)	
DPhPC/C16	14.0 ± 0.3 (n=5)	12.4 ± 0.5 (n=4)	N/A	$N_d(V) = 220V^2 + 10$
DOPC/C16	5.9 ± 0.3 (n =5)	56.5 ± 0.5 (n =4)	40 ± 0.7 (n =3)	$N_d(V) = 220V^2 + 17$

perform a series of experiments to quantify the dynamic changes in membrane geometry (area and thickness) and area-normalized channel density as a function of voltage. The dynamics and sensitivities of these variables are assessed by applying stepwise voltages. Membrane area is tracked via bottom view images of the AES, and membrane capacitance is determined from the amplitude of ac current induced by a superimposed ac voltage [42, 56].

Figure 2A shows a representative measurement of dynamic membrane area normalized to its zero-volt initial value, A_0, for a 200 mV, 10 mHz sinusoidal bias. The hysteresis observed here suggests that voltage-driven variations in channel density are not alone in causing the observed *I-V* hysteresis. Similar to the responses in Figure 1E, dynamical variations and hysteresis become very small at frequencies higher than 100 mHz (Figure 2A). And while hysteresis disappears at frequencies below 1 mHz (not shown), nonlinear quasi-static changes with respect to voltage become maximal at low frequencies [42].

Stepwise changes (0 to +200 mV) in voltage yield exponential rises in area (Figure S4), which we used to determine the characteristic time constant for EW, τ_{ew}, for the two lipids and oils (Table 1). These results indicate that EW-induced growth in membrane area is faster for DOPC lipids compared to DPhPC, and for C10 compared with C16. The former is likely the result of greater lipid acyl chain flexibility and mobility that enables faster oil exclusion and rearrangement upon bilayer formation [57], while the latter is the result of lower viscosity in C10 [42]. At equilibrium, bilayer area increases linearly with respect to the square of voltage (i.e. polarity does not matter) [55, 56, 58] , where the slope, α, denotes the EW coefficient. The data in Figure 2B and the average α values in Table 1 show that DOPC membranes in both C10 and C16 exhibit larger fractional changes in area with voltage compared to DPhPC membranes. Further, DOPC membranes formed with droplets in C16 exhibit a slightly higher area change than those formed with droplets submerged in C10. These differences are likely the result of DOPC membranes having higher monolayer and bilayer tensions and, thus, smaller zero-volt areas, which we show in Figure S5 results in larger fractional increases in bilayer area with voltage.

We also assess changes in the hydrophobic thickness of these membrane AES by measuring the specific capacitance of the membrane versus bias using a method described elsewhere [56, 59]. Figure 2C shows that gramicidin-doped DPhPC membranes in C16 exhibit relatively constant membrane thickness versus voltage up to |160mV|, whereas gramicidin-decorated DOPC membranes in both C10 and C16 become significantly thinner (15% and 30%, respectively) at higher biases. In the absence of gramicidin, DOPC membranes are also relatively thicker at zero volts, which is attributed to greater oil retention in the hydrophobic region of the membrane upon bilayer

formation compared with DPhPC as shown for lipid-only membranes in Figure S6. The larger initial thickness and steeper reduction in thickness with voltage for C10 is due to the fact that smaller molecule oils are retained in larger fractions in lipid bilayers [42, 60]. These trends, along with the fact that no significant change in thickness is recorded for DPhPC membranes containing <10% C16 by volume [42, 56], suggest that EC alters the thickness by compressive oil exclusion, not distortion or compression of the lipid molecules themselves [42]. While not shown, we have previously demonstrated that this mechanism for thickness reduction occurs on time scales of 5-25 s, slower than changes in area by EW [42].

The conducting unit in our system consists of a dimer (D) formed by two gramicidin monomers (M), aligned end-to-end across the thickness of the membrane [61-63]. Dimerization can be written as a reversible reaction given by,

$$M + M \rightleftharpoons D, \tag{1}$$

with separate forward and reverse reaction rate constants, k_R and k_D, respectively, that depend on membrane composition, temperature, ion concentration, etc. [44]. The accumulation of dimers (per unit area) in the system is thus given by:

$$\frac{dN_D}{dt} = k_R {N_M}^2 - k_D N_D. \tag{2}$$

Assuming the total concentration (mol/cm^2) of gramicidin in the interface is conserved ($N = N_M + 2N_D$), the population of gramicidin in each leaflet of the bilayer reaches an equilibrium of non-conducting (M) and conducting (D) units at fixed conditions.

Gramicidin channel formation does not require voltage, however prior research has established that k_R and k_D do vary with voltage. As a result, changing the voltage causes a transient reorganization of M and D to establish a new equilibrium in the system, where the time constant of this transient depends on the nominal values of k_R and k_D. Specifically, the fraction of conductive channels in a membrane increases with decreasing membrane thickness [64]—signifying that k_R increases with voltage [44]. Because k_D also decreases with increasing voltage [44], the speed of dimer formation (dN_D/dt) also increases at higher applied biases and at high peptide concentrations. With C16 (i.e., constant thickness), and at the relatively high peptide concentrations used in our study, channels insert in the absence of voltage and reach equilibrium at all fixed voltage levels in less than 5 ms (Figure S7). This is considerably faster than the kinetics observed by Bamberg and Läuger, in which a peptide concentration of only 2 nM was used [44].

These trends, along with the thinning responses in Figure 2C, are consistent with the likelihood that an increase of the applied voltage in our system favors a higher density of channels in the membrane, and thus higher conductivity. To confirm and quantify this relationship, we measure the nominal current at equilibrium through our gramicidin doped membranes at multiple potentials. Dividing the current by the product of the applied potential, V, the unit conductance of one dimer, G_u, and the equilibrium area of the membrane at each voltage allows us to compute the channel density per unit area versus voltage (see Figure 2D and Figure S8). Here, we see that channel density increases linearly with respect to voltage squared and that a DOPC membrane in decane exhibits a larger fractional increase in channel density compared to either DOPC or DPhPC bilayers in C16. This finding is consistent with the fact that DOPC membranes in C10 retain more oil and, thus, exhibit greater fractional decreases in thickness with increasing voltage. The nominal

data in Figure S8 also highlight the higher number of dimers in DOPC bilayers versus DPhPC and the higher number of channels in DOPC for C16 versus C10. The former is consistent with prior work [49, 50] which demonstrated a higher affinity of gramicidin with unsaturated DOPC lipids compared to DPhPC lipids, while the latter agrees with results by Hladky and Haydon which demonstrated that thinner membranes yield higher association rate constants and more dimers at equilibrium [47].

Based on these data, it is clear that both voltage-driven growth (fractional) in membrane area, A_m, and channel density, N_D, are the two states that influence the total nominal conductance, G, of the membrane as given by:

$$I = G(N_D,A_m)V. \tag{3}$$

Without a direct relationship between thickness and channel density, we perform linear regressions on the equilibrium channel density data provided in Figure S7 and use these steady-state empirical expressions to identify the initial channel densities at 0 mV, N_{D0}, and voltage dependences, m, as given by:

$$N_D(V) = N_{D0}(mV^2 + 1) \tag{4}$$

Because the channels exhibit nearly instantaneous responses to changes in voltage (and thickness) (Figure S7), the time constant for electrocompressive thinning ($O \sim s$), τ_{ec}, dictates the speed by which changes in channel density occur as a result of voltage-induced reductions in thickness. This allows us to write an empirical first order differential equation of the form:

$$\frac{dN_D}{dt} = \frac{1}{\tau_{ec}}\left(N_{D0}(mV^2 + 1) - N_D\right) \tag{5}$$

to describe the dynamic changes in N_D. For DPhPC bilayers in hexadecane which do not undergo EC, Equation 4 is used to define channel density at all points in time. Similarly, values of α and τ_{ew} (Table 1) are used as before [65] to describe the dynamic fractional area growth versus voltage, given by:

$$\frac{dA_m}{dt} = \frac{1}{\tau_{ew}}\left(\alpha v^2 - A_m(t)\right). \tag{6}$$

Given that the total number of channels in the membrane is the product of nominal membrane area, $A = A_0(1 + A_m)$ and N_D, and the unit conductance of each channel is G_u, the nominal conductance is written as

$$G(V,t) = G_u \times N_D(V,t) \times A_0(1 + A_m(V,t)) \tag{7}$$

where A_0 is the area of the interface at zero bias.

Using Equations 4-7 and values in Table 1, we simulate dynamic changes in channel density and membrane area in response to a sinusoidal voltage and use these to compute the total current. Figure 3A shows the changes in N_D and A_m versus time for a DPhPC AES formed in C16 subjected to a 10 mHz, 200 mV sinusoidal voltage. Without significant changes in thickness, the voltage induced changes in channel densities occur nearly instantaneously, which causes the dynamic response to remain in phase with the applied voltage. EW-driven changes in membrane area occur more slowly (~14 s), resulting in a noticeable time lag behind the applied potential and causing a dc shift of ~+25%. At steady state, the amplitudes of normalized channel density and membrane area are 90% and ~20%, respectively. But for AES that undergo significant thinning with increased voltage (e.g., a DOPC AES in C10), changes in N_D are slower than those in A as seen in Figure 3B. Note that this occurs because the rate of thinning limits the speed of gramicidin insertion in the membrane. Figure 3C and Fig S9 show the simulated nominal current versus voltage and time, respectively, at steady state for the same sinusoidal voltage input. Here, we see the models accurately capture the nonlinear changes in synaptic conductance that affect the induced current.

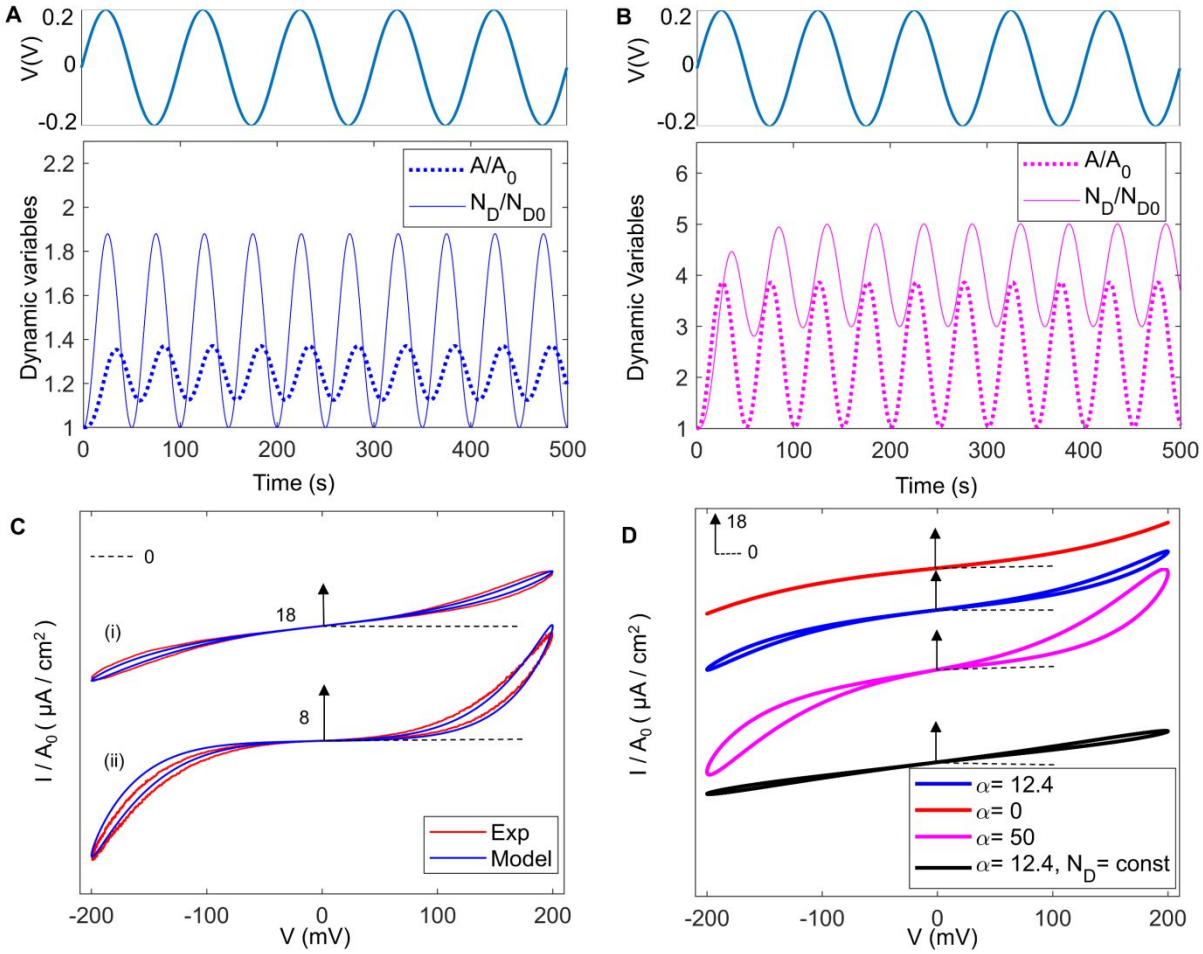

Figure 3. Simulated dynamic responses of AES. Membrane area and channel density using EW and EC parameters for a DPhPC membrane in C16 (A) and DOPC in C10 (B), respectively, in response to 200 mV, 10 mHz sinusoidal voltage (top). Simulated *I-V* relationships for: (C) (i) DPhPC AES in C16, and (ii) DOPC AES in C10; and (D) DPhPC AES in C16 at various electrowetting conditions with dynamic channel density. The black trace in (D) predicts the response of the device at a constant channel density. Vertical scales denoted using arrow length and value. All currents are normalized per zero-volt initial area, A_0. Applied bias consisted of a 200-mV bipolar sinusoidal voltage at 10 mHz, unless stated otherwise.

In Figure 3D, we simulate the *I-V* response of a DPhPC AES in C16 at 10mV for varying α values to investigate the sources of nonlinearity and hysteresis. By setting α to zero (i.e., area is fixed), hysteresis vanishes and the nonlinear increase in current is explained by the instantaneous growth in channel density with voltage. Increasing α to a value of 50 amplifies both the total change in current and the hysteresis during a voltage. Further, keeping α at the measured value of 12.4 and setting N_D to be constant yields in a nearly linear *I-V* relationship with only a small amount of hysteresis. In contrast, the larger, slow increases in N_D for DOPC AES add additional *I-V* hysteresis and nonlinearity due to time-varying channel densities independent of the membrane area.

Short-term facilitation and depression in AES. Activity-dependent short-term plasticity (STP) enables synapses to adjust their conductance strength in ways that either facilitate (strengthen) or depress (weaken) the activity of the post-synaptic neuron. The *I-V* hysteresis demonstrated in Figure 2 shows that at specific frequencies the AES exhibits a conductance that is dependent both on the present value and prior history of applied voltage. Because these hysteresis loops disappear at very low frequencies, the system can be classified as a volatile memristor for which the alterations in conductance return to an equilibrium level upon removal of the excitation. The prior section demonstrates that for gramicidin-doped bilayers with symmetric lipid compositions these alterations occur due to reversible increases in both area and channel density, processes that occur at characteristic time scales governed by the dynamics of EW and EC, respectively.

Plasticity of synaptic elements is commonly assessed by recording the responses to multiple, successive voltage excitations [66]. Therefore, we stimulate our AES with a train of positive, rectangular voltage pulses and study the dynamic current responses. As compared in Figure 4A, we consider gramicidin-doped AES membranes that have either symmetric and asymmetric lipid compositions—the latter, which we have previously shown can be used to enable asymmetric EW responses with respect to 0 mV [42]. Specifically, we compare the behaviors of a symmetric DOPC bilayer in decane to an asymmetric membrane consisting of one DOPC leaflet and one leaflet containing a 1:1 molar mixture of DOPC and 1,2-di-O-phytanoyl-sn-glycero-phosphocholine (DOPhPC)—a combination that exhibits an intrinsic dipole potential difference of -85 mV. Unlike a symmetric membrane that exhibits zero intrinsic potential, the net potential across an asymmetric membrane is the sum of the applied voltage and the intrinsic potential [42]. This means that EW and EC are minimized when the applied potential is equal and opposite to the intrinsic potential, not at zero. Thus, the asymmetric membrane is larger in area and thinner at 0 mV than when +85 mV is applied. Here, we hypothesize that a voltage-dependent reduction in area and increase in thickness can be used to lessen the number of conductive channels in the membrane, thereby creating a depressive form of short-term plasticity.

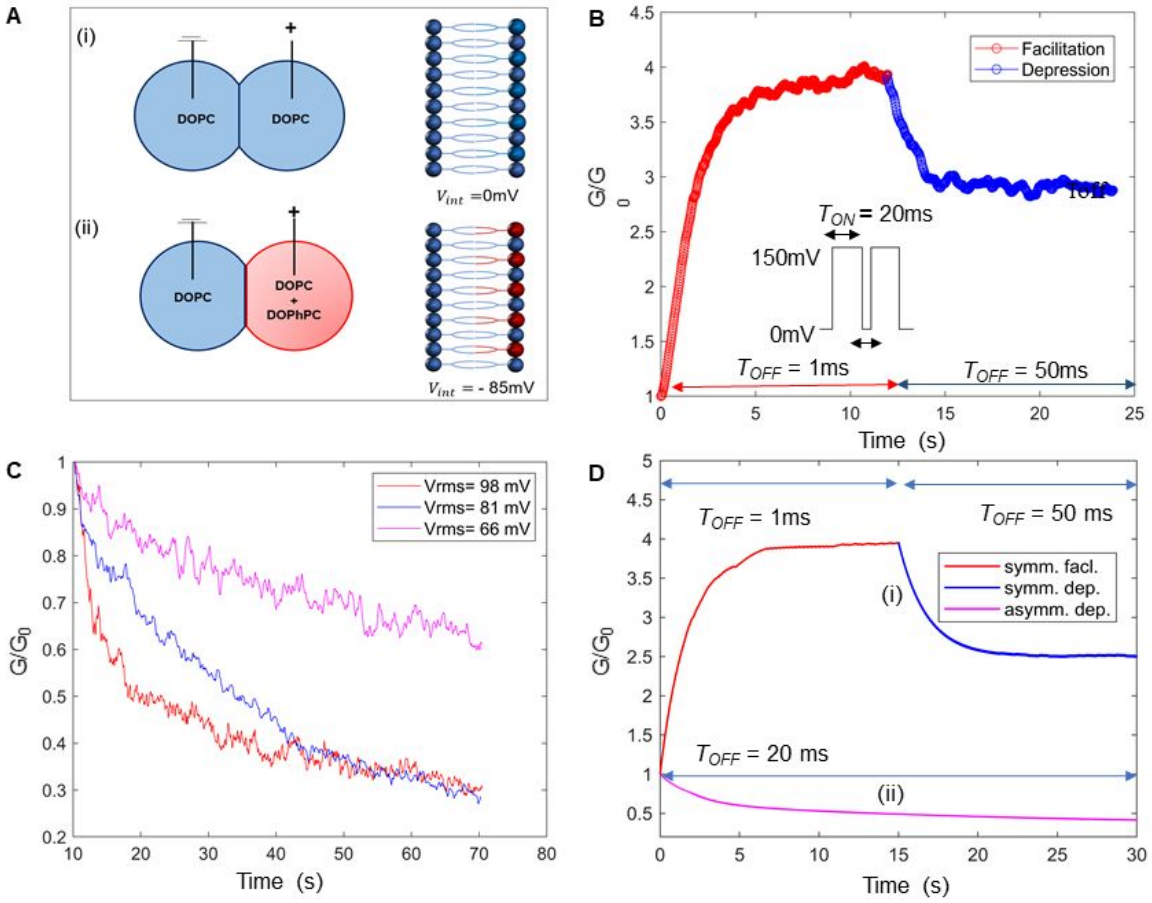

Figure 4. Short term plasticity in symmetric and asymmetric AES. (A) Cartoon depicting symmetric and asymmetric assembly of droplets and the interfacial membrane. (B) Accumulation and depression of current per unit area of the membrane (facilitation and depression) for varying T_{OFF} values. (C) Depression of conductance of the device even with increased stimuli (voltage input) because of reverse electrowetting stemming from dipole potential difference of asymmetric droplets. (D) Simulation of short-term facilitation and depression in symmetric (blue lines) and asymmetric AES (magenta line).

Figure 4B shows the raw ohmic current measured across a symmetric gramicidin doped DOPC membrane in response to +150 mV, 50 ms ON pulses followed by 0 mV OFF periods. For the first 10 s when the OFF time is 1 ms (95.2% duty cycle, V_{RMS} = 95 mV), the peak current during ON times (normalized by the zero-voltage area) increases exponentially across many pulses with a time constant of 1.75 s. This type of facilitative short-term plasticity is consistent with the time for gramicidin channels/bilayer area to increase in response to a non-zero RMS voltage. With sufficient preceding rise in synaptic conductance, a change in the OFF time of the pulses to 50 ms (28.5% duty cycle, V_{RMS} = 29 mV) causes the membrane to gradually become less conductive as indicated by the reduction in ohmic current in Figure 4B after 10 s. This depressing response occurs as the area of the membrane drops, the thickness increases, and the channel density lowers a smaller positive RMS voltage. However, the fact that the steady-state peak current for 50 ms OFF times is still higher than the initial value prior to pulse train excitation means that if only this

stimulus were provided instead, a symmetric membrane will not exhibit depressive STP without sufficient facilitative STP first occurring.

Yet, depression in electrical synapses is more common [10, 67], a trait that enables modulation of electrical coupling [67], regulates response to the sensory surround and arousal states [10]. Figure 4C shows the peak ohmic current versus time for an asymmetric DOPC: DOPC+DOPhPC membrane containing gramicidin at three different positive V_{RMS} levels (varying duty cycle, equal amplitude). Representative *I-V* measurements for an asymmetric AES are provided in Figure S10. Here, unlike the response in Figure 4B, we observe that current only decreases upon application of a positive voltage. This occurs because the net membrane potential drops when voltage increases from 0 mV to +100 mV. The amount of decrease varies with the RMS value, which is consistent with the idea that the membrane becomes least conductive (see Figure S10) when the area is small and the thickness is large which occurs at zero net potential. Quasi-static analysis (Figure S11) confirms that the interfacial area of an asymmetric AES responds to the transmembrane potential difference. However, we also observe the channel density to exhibit stronger increases with voltage at negative applied potentials, where the net membrane potential is larger, compared to positive stimuli. This effect is likely a combination of channel kinetics changing with the applied potential and the thickness of the membrane varying with respect to net membrane potential.

Figure 4D (i) and (ii) show simulated peak currents for symmetric and asymmetric AES subjected to unipolar square pulse inputs (150 mV, 20 ms ON, 0 mV, variable duration T_{OFF}). These trends bear close resemblance to the measured behaviors of symmetric and asymmetric AES devices as seen in Figure 4B-C. For the asymmetric system, the voltage dependent channel density equation (Equation 5) and electrowetting equation (Equation 6) are modified to accommodate a net bias input of $v = v_{appl} + v_{int}$.

AES enable variable synchronization of neurons

Electrical synapses synchronize the activities of many neurons [68, 69] by allowing fast, threshold-independent sharing of action potentials and ionic gradients. The AES presented in this paper share several traits in common with ES, including a variable conductance that occurs at biologically relevant levels of voltage and which spans nominal conductance ranges similar to ES. Therefore, to demonstrate that our voltage-dependent AES can synchronize neurons, we employ our model of AES conductance and simulate in MATLAB the responses of two Hodgkin-Huxley (H-H) neurons [70] connected by our adaptive AES (illustrated in Figure 5A). The variable resistances in the
neurons represent the voltage-gated sodium and potassium channels in addition to leakage pathways. The neuron on the left is stimulated with a dc current density of 10 μA/cm^2, a level which is sufficient to elicit repeated oscillations. This injection charges neuron 1, whereby at a sufficient voltage the sodium channels open in neuron 1, causing rapid depolarization of the cell. Then, at sufficiently positive voltage, potassium channels open, hyperpolarizing the cell and resetting the voltage. This nonlinear, oscillatory response creates an action potential with a spiking period of 15 ms. By connecting two neurons with a threshold-independent AES, some of the injected current can also enter neuron 2, where it can similarly charge and fire. The amount of current through the AES depends on its conductance, which in this application is modulated by the relative neuron voltages, V_1 and V_2. For these simulations, we use the parameters defined in Supplementary Table 1 for a gramicidin doped DOPC membrane in C10. The voltage-dependent

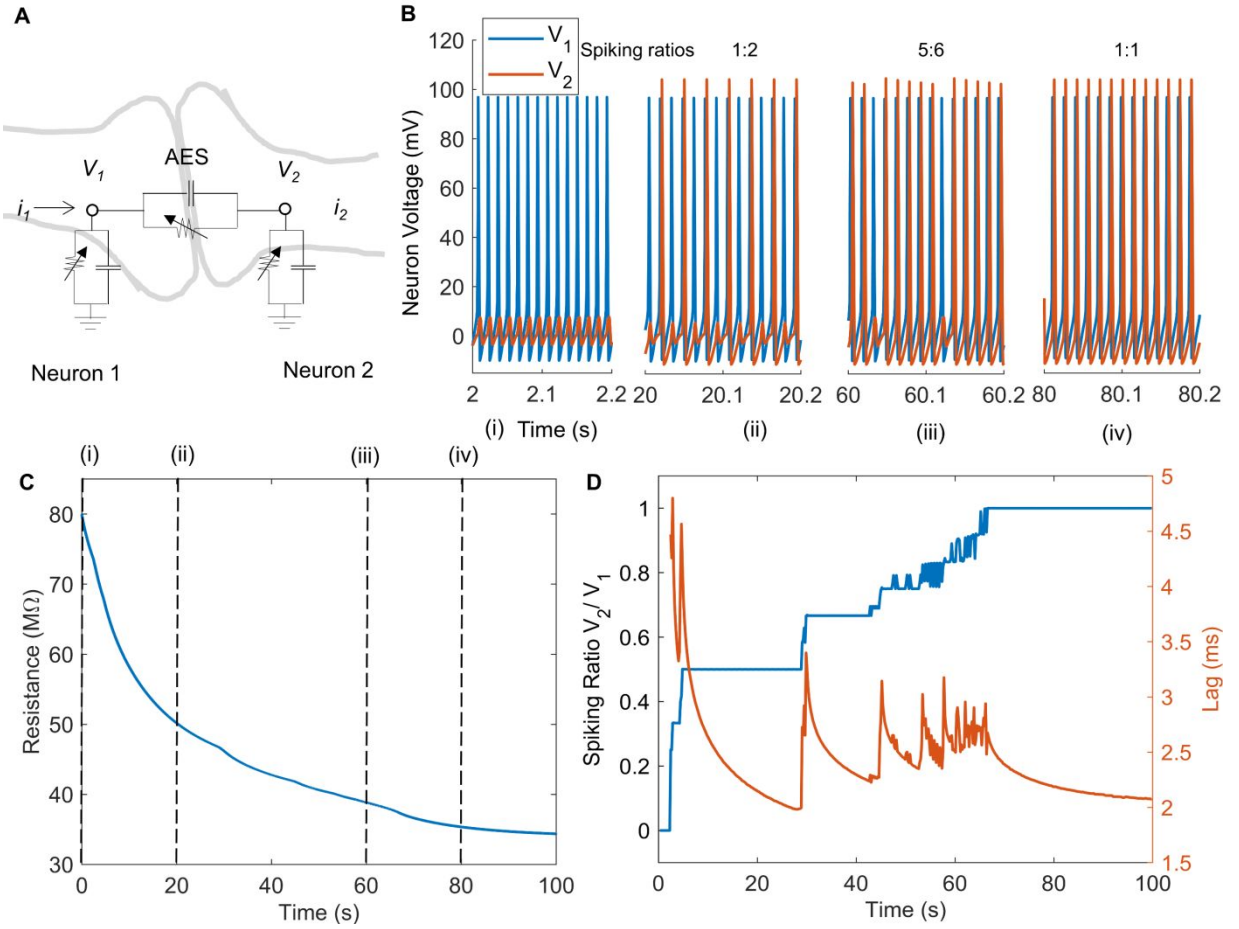

Figure 5. HH neuron synchronization through AES plasticity. (A) Illustration of two HH neurons joined by an AES. (B) Simulated neuron voltages versus time in response to a constant injected current into Neuron 1. (C) AES resistance versus time during adaption. (D) Neuron voltage spiking ratios and lag time between neuron spikes versus time.

membrane capacitance of the AES (C_m = 0.496 μF/cm^2) is also included in the calculation, and we assume the active areas of the neuron and synapse (zero-volt area) are equal to the DIB area (3.3 x 10^{-4} cm^2) observed in experiments.

Figure 5B shows the simulated voltages of both neurons versus time; Figures 5C-D show the computed nominal resistance of the AES and the spiking ratios (spike count of neuron 2 to that of neuron 1) and time lag between adjacent spikes, respectively. The simulation shows that only neuron 1 produces an action potential (Figure 5B (i)). The initial AES resistance (~80 MΩ) limits charging of neuron 2, resulting in only sub-threshold oscillations with amplitudes of 6-8% of V_1. This response shows that initially neuron 2 is completely desynchronized from action potentials from neuron 1.

However, over time the difference in neuron voltages (38 mV RMS) lowers the resistance of the AES to reduce to ~34 MΩ via bilayer area growth and increased channel density (Fig S12). Neuron 2 begins generating action potentials when the AES resistance falls below 74 MΩ. This voltage-dependent adaptation allows increasingly more current to enter neuron 2 and further increases the

rate of action potential generation. Figure 5B (ii-iv) show this adaptation; here we see neuron 2 exhibiting action potentials with increasing frequency over time (total simulation time is 100 s to capture the full adaptation of the AES). The spiking ratio increases incrementally during this time, where after approximately 67 s, when the AES resistance drops below ~40 MΩ, every action potential by neuron 1 coincides with one from neuron 2. While synchronized in frequency at this point, action potentials from neuron 2 still lag by ~2 ms those from neuron 1. This time lag decreases non-monotonically during the AES adaptation; specifically, it appears to decrease exponentially in time for each period of constant spiking ratios.

An electrical synapse mimic for synchronizing spiking neurons—e.g., for use in artificial neural networks—has real advantages compared to devices mimicking the one-direction, threshold dependent variable conductance of a chemical synapse. The bidirectional conductance of the AES means that if neuron 2 were stimulated with current instead, neuron 1 could become synchronized. Additionally, the lack of a voltage-threshold for ion channel formation allows ions to quickly pass through the AES to charge and fire neuron 2 with minimal lag. In contrast, a memristive synaptic mimic constructed using alamethicin [65] exhibits much slower channel insertion kinetics, which would prevent successful synchronization of the two neurons.

The simulation shows how the voltage-dependent plasticity of an AES can be used to adaptively couple spiking neurons, and the conditions for the calculations require some tuning to demonstrate this functionality. Specifically, initial channel density, N_{D0}, and the voltage dependency, m, of the synapse are set to 6.5 x 10^6 and 2 x 10^9, respectively, to ensure that the device exhibited an initial resistance of 80 MΩ and a large reduction in resistance at RMS voltages below 50 mV. In contrast, smaller values of N_{D0} and m (such as those in Table 1) result in a highly resistive junction that does not sufficiently reduce to cause firing in neuron 2. Nonetheless, the parameters used closely match experimentally obtained values on a symmetric DOPC membrane in C10 by mechanically reducing the membrane area after bilayer formation (see Supplementary Table S1 for measured values and Figure S5 for effect of membrane area on electrowetting sensitivity). In contrast, while an asymmetric AES displays short-term depression under a sufficiently large positive potential (see Figure 4C in the manuscript), the same device is unable to desynchronize H-H neurons because the average voltage across a highly conductive AES (required to synchronize neurons) is insufficient for appreciably changing AES. Figures S13 summarizes the response of an initially conductive AES placed between two Hodgkin-Huxley neurons.

In our simulation, the ratio of neuron area to synapse area is a parameter that strongly impacts the amount of nominal current flowing through the AES. This is based on the fact that Hodgkin-Huxley equations are normalized per area of the neuron membrane. Therefore, when the active area of the neuron is larger than that of the synapse, the synapse is considerably less conductive than the neurons. This change means that even less current passes through the AES, lowering the rate of firing of neuron 2. Less current through the AES also causes the V_{RMS} difference between the neurons to shrink to 27 mV, which subsequently results in a smaller voltage-induced plasticity. Furthermore, higher neuron conductance means even larger reductions in AES resistance from the same initial value (80 MΩ) are needed to fully synchronize the two neurons. For example, increasing the area ratio to just 10 raises the final synapse resistance to 50 MΩ, a value that now only results in sub-threshold voltage oscillations in neuron 2. This demonstrates that effectively matching the impedances of the neurons and the adjoining synapse is important for making use of voltage-activity plasticity in hardware-based neural circuits.

CONCLUSION

We present a threshold-independent, artificial electrical synapse that exhibits volatile memristance and which mimics the composition, structure, and transport properties of an electrical synapse found in the mammalian brain. Our unique, two-terminal AES consists of a lipid bilayer membrane doped with gramicidin peptides that form conductive ion channels through the lipid bilayer. Like connexins in ES, these channels feature an end-to-end connection across both leaflets of the membrane and do not require a threshold-voltage to conduct ions. The current-voltage relationships of gramicidin-based AES exhibit pinched hysteresis at excitation frequencies between 10-100 mHz. Experiments reveal that the volatile memristive device is affected by two voltage-dependent state variables: the gramicidin channel concentration per unit area and membrane area, the product of which dictate the total number of channels in the AES and, thus the conductance of the device. In addition, the current-voltage relationships show that combinations of peptide concentration, oil composition, and lipid type and arrangement modulate the conductivity, nonlinearity, and hysteresis of the AES. Using a mathematical model of AES developed from empirical expressions for both state variables, we also show that the voltage-induced plasticity in an AES can dynamically synchronize the firing of two HH neurons, illustrating one of the key uses of ES in neural networks.

Like the brain, ES functionality in neural networks may also enable greater cognitive power in neuromorphic circuits. Our AES devices, unlike most neuromorphic devices, mimic the continuously-variable conduction, bidirectional ion transport, and activity-dependent plasticity of ES. These results also highlight that a biomolecular approach is one that enables uniquely modular transport properties and tunable plasticity that can be achieved at biologically relevant voltages.

EXPERIMENTAL

Materials. The aqueous droplets in each DIB-based AES consist of phospholipid vesicles, salt, and buffering agent in 99.99% pure deionized water. Sodium chloride (NaCl), 3-(N0morpholino) propanesulfonic acid (MOPS), sodium hydroxide (NaOH), agarose ($C_{12}H_{18}O_9$), *n*-hexadecane (99% pure), *n*-decane (99%pure), ethanol, isopropyl alcohol was purchased from Sigma Aldrich. DPhPC, DOPC, and DOPhPC lipids are obtained from Avanti Polar Lipids, Inc and used without further purification. Lipid vesicles are prepared and stored at a concentration 2 mg/ml in aqueous buffer containing 500 mM NaCl, 10 mM MOPS at pH of 7.0 achieved via NaOH titration as described elsewhere [55]. Hydrogel (2% (w/v)) electrode coatings are prepared from agarose powder and the same buffer. A stock solution of gramicidin in ethanol (10 mg/mL) is diluted with the lipid vesicle solutions to yield the desired final concentration.

Methods for DIB formation. DIBs are formed between two, 300 nL aqueous droplets suspended agarose coated wire-type electrodes in an oil-filled reservoir as described elsewhere [71]. The oil reservoir and droplets are centered above a 4X objective lens on an Olympus IX50 inverted microscope. The positions of both electrodes are controlled by three-axis micromanipulators. A lipid bilayer forms spontaneously within a minute after bringing droplets into contact following a brief incubation period to ensure lipid monolayer assembly. Bottom-view images (Figure 1B) of DIB-based AES obtained using a QIClick-F-M-12-C (SN: Q31274) camera controlled by MicroManager software are used to estimate membrane area for computing specific capacitance and thickness. Based on the work by Taylor et al [55], a correction factor of 1.773 is used to account for membrane ellipticity due to sagging droplets.

Electrical Measurements. Current measurements are made using an Axopatch 200B patch clamp amplifier and Digidata 1440 data acquisition system (Molecular Devices). All recordings are made at room temperature with appropriate shielding using a well-grounded Faraday cage in place to minimize noise. Necessary input voltage waveforms are generated using Hewlett-Packard 3314A function generator and customized LabVIEW VI codes with NI four channel analogue output module (NI 9263). Outputs from these sources are input to the headstage of the Axopatch 200B through the external input to the amplifier. Confirmation of bilayer formation and measurements of nominal capacitance stems from the bilayer's current response to a 10 mV, 350 Hz triangular voltage waveform input as discussed earlier [55]. Sinusoidal cyclic voltammetry scans at various sweep rates are performed on the bilayer to generate the *I-V* relationships [72]. The pinched hysteretic loops presented in Figure 1 are obtained after filtering the residual capacitive current resulting from the lipid membrane as described elsewhere [73]. The short-term plasticity behavior is studied using rectangular voltage pulses at varying duty cycles.

Simulating the model. We numerically simulate the hysteretic responses and short-term plasticity of our AES and the variable synchronization of Hodgkin-Huxley neurons using the described model and measured parameters (e.g. Table 1) in MATLAB.

ACKNOWLEDGEMENTS

Financial support was provided by the National Science Foundation Grant NSF ECCS-1631472 and the Air Force Office of Scientific Research Multi University Research Initiative Grant FA9550-19-1-0213.

REFERENCES

1. L. O. Chua, *Proceedings of the IEEE*, 2003, **91**, 1830-1859.
2. L. Chua, *IEEE Transactions on Circuit Theory*, 1971, **18**, 507-519.
3. M. D. Ventra, Y. V. Pershin and L. O. Chua, *Proceedings of the IEEE*, 2009, **97**, 1717-1724.
4. Y. ZhenYu, T. Heng, C. GuanHua and L. O. Chua, *IEEE Transactions on Circuits and Systems II: Express Briefs*, 2015, **62**, 402-406.
5. M. A. Colicos, in *Encyclopedia of Neuroscience*, eds. M. D. Binder, N. Hirokawa and U. Windhorst, Springer Berlin Heidelberg, Berlin, Heidelberg, 2009, DOI: 10.1007/978-3-540-29678-2_74, pp. 50-52.
6. D. B. Strukov, G. S. Snider, D. R. Stewart and R. S. Williams, *Nature*, 2008, **453**, 80-83.
7. T. Prodromakis, C. Toumazou and L. Chua, *Nature Materials*, 2012, **11**, 478.
8. Y. Li, Z. Wang, R. Midya, Q. Xia and J. J. Yang, *Journal of Physics D: Applied Physics*, 2018, **51**, 503002.
9. J. S. Haas, C. M. Greenwald and A. E. Pereda, *BMC Cell Biol*, 2016, **17 Suppl 1**, 14-14.
10. J. S. Haas, B. Zavala and C. E. Landisman, *Science*, 2011, **334**, 389.
11. J. S. Haas, *Frontiers in cellular neuroscience*, 2015, **9**, 378-378.
12. Alberto E. Pereda, *Neuron*, 2016, **90**, 912-914.
13. S. A. Bloomfield, D. Xin and T. Osborne, *Visual Neuroscience*, 1997, **14**, 565-576.
14. S. A. Bloomfield, D. Xin and S. E. Persky, *Visual Neuroscience*, 1995, **12**, 985-999.
15. B. W. Connors and M. A. Long, *Annual Review of Neuroscience*, 2004, **27**, 393-418.
16. M. V. L. Bennett, *Journal of Neurocytology*, 1997, **26**, 349-366.

17. V. L. Tawfik and P. Flood, *Anesthesiology: The Journal of the American Society of Anesthesiologists*, 2016, **124**, 13-15.
18. A. G. Purves D, Fitzpatrick D, et al., , *Neuroscience.*, Sinauer Associates, Sunderland (MA), 2nd Edition edn., 2001.
19. L. Rela and L. Szczupak, *Molecular Neurobiology*, 2004, **30**, 341-357.
20. A. E. Pereda, S. Curti, G. Hoge, R. Cachope, C. E. Flores and J. E. Rash, *Biochimica et Biophysica Acta (BBA) - Biomembranes*, 2013, **1828**, 134-146.
21. D. Debanne and M. Russier, *The Journal of physiology*, 2017, **595**, 4121-4122.
22. S. Curti and J. O'Brien, *BMC Cell Biol*, 2016, **17**, 13.
23. A. L. Harris, *Quarterly Reviews of Biophysics*, 2001, **34**, 325-472.
24. F. F. Bukauskas and V. K. Verselis, *Biochimica et Biophysica Acta (BBA) - Biomembranes*, 2004, **1662**, 42-60.
25. R. Rozental, M. Srinivas, S. Gökhan, M. Urban, R. Dermietzel, J. A. Kessler, D. C. Spray and M. F. Mehler, *Brain Research Reviews*, 2000, **32**, 57-71.
26. A. B. Belousov and J. D. Fontes, *Trends in Neurosciences*, 2013, **36**, 227-236.
27. M. Samoilova, J. Li, M. R. Pelletier, K. Wentlandt, Y. Adamchik, C. C. Naus and P. L. Carlen, *Journal of Neurochemistry*, 2003, **86**, 687-699.
28. M. E. Spira and M. V. L. Bennett, *Brain Research*, 1972, **37**, 294-300.
29. T. J. Carew and E. R. Kandel, *Science*, 1976, **192**, 150.
30. Y. Lefler, Y. Yarom and Marylka Y. Uusisaari, *Neuron*, 2014, **81**, 1389-1400.
31. S. W. Jaslove and P. R. Brink, in *Cell-to-Cell Communication*, ed. W. C. De Mello, Springer US, Boston, MA, 1987, DOI: 10.1007/978-1-4613-1917-7_4, pp. 103-147.
32. A. Chiolerio, M. Chiappalone, P. Ariano and S. Bocchini, *Frontiers in neuroscience*, 2017, **11**, 70-70.
33. J. J. Yang, M. D. Pickett, X. Li, D. A. A. Ohlberg, D. R. Stewart and R. S. Williams, *Nature Nanotechnology*, 2008, **3**, 429.
34. R. Waser and M. Aono, *Nature Materials*, 2007, **6**, 833.
35. S. H. Jo and W. Lu, *Nano Letters*, 2008, **8**, 392-397.
36. S. H. Jo, K.-H. Kim and W. Lu, *Nano Letters*, 2009, **9**, 496-500.
37. Y.-E. Syu, T.-C. Chang, J.-H. Lou, T.-M. Tsai, K.-C. Chang, M.-J. Tsai, Y.-L. Wang, M. Liu and S. M. Sze, *Applied Physics Letters*, 2013, **102**, 172903.
38. Z. Lv, Y. Zhou, S.-T. Han and V. A. L. Roy, *Materials Today*, 2018, **21**, 537-552.
39. N. Duan, Y. Li, H.-C. Chiang, S.-P. Huang, K.-S. Yin, J. Chen, C.-I. Yang, T.-C. Chang and X.-S. Miao, *ACS Applied Electronic Materials*, 2019, **1**, 132-140.
40. S. K. Südhof T.C., in *Pharmacology of Neurotransmitter Release. Handbook of Experimental Pharmacology*, Springer, Berlin, Heidelberg, 2008, vol. 184.
41. D. Berco, Y. Zhou, S. R. Gollu, P. S. Kalaga, A. Kole, M. Hassan and D. S. Ang, *ACS Nano*, 2018, **12**, 5946-5955.
42. J. S. Najem, M. S. Hasan, R. S. Williams, R. J. Weiss, G. S. Rose, G. J. Taylor, S. A. Sarles and C. P. Collier, *Nature Communications*, 2019, **10**, 3239.
43. J. S. Najem, G. J. Taylor, R. J. Weiss, M. S. Hasan, G. Rose, C. D. Schuman, A. Belianinov, C. P. Collier and S. A. Sarles, *ACS Nano*, 2018, **12**, 4702-4711.
44. E. Bamberg and P. Läuger, *The Journal of Membrane Biology*, 1973, **11**, 177-194.
45. N. R. Clement and J. M. Gould, *Biochemistry*, 1981, **20**, 1544-1548.
46. M. E. Johnson, S. Simon, J. W. Kauffman and R. C. Macdonald, *Biochimica et Biophysica Acta (BBA) - Biomembranes*, 1973, **291**, 587-591.
47. S. B. Hladky and D. A. Haydon, *Biochimica et Biophysica Acta (BBA) - Biomembranes*, 1972, **274**, 294-312.

48. O. S. Andersen, *Biophys J*, 1983, **41**, 119-133.
49. J. M. Muller, G. van Ginkel and E. E. van Faassen, *Biochemistry*, 1996, **35**, 488-497.
50. J.-M. Camaleńo-Delgado, X. K. Zhao and J. H. Fendler, *Canadian Journal of Chemistry*, 1990, **68**, 888-896.
51. L. O. Chua and K. Sung Mo, *Proceedings of the IEEE*, 1976, **64**, 209-223.
52. H. Kim, M. Pd. Sah and S. Adhikari, *Pinched Hysteresis Loops is the Fingerprint of Memristive Devices*, 2012.
53. L. Chua, *Applied Physics A*, 2011, **102**, 765-783.
54. Y. Y. Flood Sung, Li Zhang, Tao Xiang, Philip H.S. Torr, Timothy M. Hospedales *IEEE/CVF Conference on computer vision and pattern recognition*, 2018, 1199-1208.
55. G. J. Taylor, G. A. Venkatesan, C. P. Collier and S. A. Sarles, *Soft Matter*, 2015, **11**, 7592-7605.
56. L. C. M. Gross, A. J. Heron, S. C. Baca and M. I. Wallace, *Langmuir*, 2011, **27**, 14335-14342.
57. G. A. Venkatesan, J. Lee, A. B. Farimani, M. Heiranian, C. P. Collier, N. R. Aluru and S. A. Sarles, *Langmuir*, 2015, **31**, 12883-12893.
58. S. H. White and T. E. Thompson, *Biochimica et Biophysica Acta (BBA) - Biomembranes*, 1973, **323**, 7-22.
59. S. H. White, *Biophys J*, 1978, **23**, 337-347.
60. T. J. McIntosh, S. A. Simon and R. C. MacDonald, *Biochimica et Biophysica Acta (BBA) - Biomembranes*, 1980, **597**, 445-463.
61. E. Bamberg, H. J. Apell and H. Alpes, *Proc Natl Acad Sci U S A*, 1977, **74**, 2402-2406.
62. D. W. Urry, *Proc Natl Acad Sci U S A*, 1971, **68**, 672-676.
63. T. L. Jones, R. Fu, F. Nielson, T. A. Cross and D. D. Busath, *Biophys J*, 2010, **98**, 1486-1493.
64. E. Bamberg and R. Benz, *Biochimica et Biophysica Acta (BBA) - Biomembranes*, 1976, **426**, 570-580.
65. G. J. T. Joseph S. Najem, Charles P. Collier and Stephen A. Sarles., *ACS Appl Mater Interfaces*, 2018.
66. C. F. Stevens and Y. Wang, *Neuron*, 1995, **14**, 795-802.
67. C. E. Landisman and B. W. Connors, *Science*, 2005, **310**, 1809.
68. J. C. Magee and D. Johnston, *Science*, 1997, **275**, 209.
69. R. G. M. Morris, *Brain Research Bulletin*, 1999, **50**, 437.
70. A. L. Hodgkin and A. F. Huxley, *The Journal of physiology*, 1952, **116**, 449-472.
71. G. J. Taylor and S. A. Sarles, *Langmuir*, 2014, **31**, 325-337.
72. J. S. Au - Najem, G. J. Au - Taylor, N. Au - Armendarez, R. J. Au - Weiss, M. S. Au - Hasan, G. S. Au - Rose, C. D. Au - Schuman, A. Au - Belianinov, S. A. Au - Sarles and C. P. Au - Collier, *JoVE*, 2019, DOI: doi:10.3791/58998, e58998.
73. T. Okazaki, M. Sakoh, Y. Nagaoka and K. Asami, *Biophys J*, 2003, **85**, 267-273.

An artificial electrical synapse that mimics the structure, transport properties, and plasticity of biological electrical synapses exhibits voltage-controlled memristance by exploiting reconfigurable membrane geometry.